Advances in Concrete Construction, *Vol. 1, No. 4 (2013) 341-358*
DOI: http://dx.doi.org/10.12989/acc.2013.1.4.341

Evaluation of mechanical properties for high strength and ultrahigh strength concretes

A. Ramachandra Murthy*[1], Nagesh R. Iyer[1] and B.K. Raghu Prasad[2]

[1]*CSIR- Structural Engineering Research Centre, Chennai 600113, India*
[2]*Indian Institute of Science, Bangalore 560012, India*

(Received July 6, 2013, Revised December 3, 2013, Accepted December 10, 2013)

Abstract. Due to fast growth in urbanisation, a highly developed infrastructure is essential for economic growth and prosperity. One of the major problems is to preserve, maintain, and retrofit these structures. To meet the requirements of construction industry, the basic information on all the mechanical properties of various concretes is essential. This paper presents the details of development of various concretes, namely, normal strength concrete (around 50 MPa), high strength concrete (around 85 MPa) and ultra high strength concrete (UHSC) (around 120 MPa) including their mechanical properties. The various mechanical properties such as compressive strength, split tensile strength, modulus of elasticity, fracture energy and tensile stress vs crack width have been obtained from the respective test results. It is observed from the studies that a higher value of compressive strength, split tensile strength and fracture energy is achieved in the case of UHSC, which can be attributed to the contribution at different scales viz., at the meso scale due to the fibers and at the micro scale due to the close packing of grains which is on account of good grading of the particles. Micro structure of UHSC mix has been examined for various magnifications to identify the pores if any present in the mix. Brief note on characteristic length and brittleness number has been given.

Keywords: high strength concrete; ultra high strength concrete; characterization; crack mouth opening displacement, fracture energy; tensile stress vs crack width

1. Introduction

Due to fast growth in urbanisation, a highly developed infrastructure is essential for economic growth and prosperity. Many structures essential to this infrastructure, especially those made of reinforced concrete (RC), have suffered severe degradation since their construction due to the combined effects of deicing salts, freeze–thaw cycles, aggressive environments, and drastically increased live loads. One of the major problems facing the civil engineers of today is to preserve, maintain, and retrofit these structures. Concrete has been one of the most commonly used building materials in the world. The historical development of concrete material may be marked and divided into several stages. The first is the traditional normal strength concrete (NSC) and followed by high strength concrete (HSC), high performance concrete (HPC) and ultra high strength concrete (UHSC) with axial compressive strength more than 100 MPa and also with a high tensile strength (more than 10% of the compressive strength) has been successfully developed

*Corresponding author, E-mail: murthyarc@serc.res.in, murthycsdg@gmail.com

http://www.techno-press.org/?journal=acc&subpage=7 ISSN:2287-5301(Print) 2287-531X(Online)

(Richard and Cheyrezy 1994, 1995, Mingzhe *et al*. 2010, Goltermann *et al*. 1997). UHSC has a distinctive advantage and great potential in a wide range of engineering applications such as blast shelters, impact resistant structures, nuclear structures, skyscrapers, corrosion proof structures and pavements. In order to improve the strength deformability and toughness of a UHSC, a number of short steel fibers are embedded to restrain cracks in the matrix. Embedding steel fibers in the matrix enhances the toughness and deformation of UHSC and overcome the disadvantage of high brittleness (Massidda *et al*. 2001, Guvensoy *et al*. 2004, Chan and Chu 2004, Shaheen and Shrive 2006, Lee *et al*. 2007).

It was reported that reactive powder concrete (RPC) has a remarkable flexural strength and very high ductility. Its ductility is about 250 times higher than that of conventional concrete (Richard and Cheyrezy 1994). Massidda *et al*. (2001) studied the effects of autoclaving under saturated vapor at 180^0C on the physical and mechanical properties of reactive-powder mortars reinforced with brass-coated steel fibers. Chan and Chu (2004) reported that incorporation of silica fume in RPC matrix remarkably enhances the steel fiber–matrix bond characteristics due to the interfacial-toughening effect upon fiber slip. Lee *et al*. (2007) used RPC as a new repair material and evaluated its bond durability to existing concrete. Wang and Lee (2007) conducted experiments on RC beam-column joint strengthened with ultra-high steel fiber reinforced concrete (UFC) under cyclic loading. Yazici *et al*. (2009) investigated mechanical properties such as compressive strength, flexural strength, and toughness of RPC produced with class-C fly ash (FA) and ground granulated blast furnace slag (GGBFS) under different curing conditions (standard, autoclave and steam curing).

For a better understanding of the fracture behavior of concrete structurestwo fracture properties of concrete are needed, namely, the specific fracture energy G_F and the corresponding tension softening relation $\sigma(w)$. The work-of-fracture method recommended by RILEM (1985) for measuring the specific fracture energy of concrete from notched three-point bend specimens of different sizes and notch to depth ratios is still the most common method used throughout the world (Pan 2011, Sahin and Koksal 2011), despite the fact that the specific fracture energy so measured is known to vary with the size and shape of the test specimen (Bazant and Kazemi 1991, Bazant 1996, Nallathambi *et al*. 1985, Carpinteri and Chiaia 1996, Hu and Wittmann, 1992). The reasons for this variation have also been known for nearly two decades, and two methods have been proposed by Elices and co-workers (Elices *et al*. 1992, Guinea *et al*. 1992, Planas *et al*. 1992) and by Hu and Wittmann (Hu and Wittmann 2000) to correct the measured size-dependent specific fracture energy (G_f) in order to obtain a size-independent value (G_F). Elices and co-workers (Elices *et al*. 1992, Guinea *et al*. 1992, Planas *et al*. 1992) identified the sources of experimental error in the RILEM method and proposed a methodology for eliminating the major source of error, namely by including the work-of-fracture that is not measured in the RILEM method due to practical difficulties in capturing the tail part of the load-deflection plot. The second method proposed by Hu and Wittmann (2000) recognized that the local specific energy varied during the propagation of a crack, the variation becoming more pronounced as the crack approached the stress-free back face boundary of the specimen. Karihaloo *et al*. (2000) and Abdalla and Karihaloo (2003) extended the free boundary effect concept of Hu and Wittmann (2000) and showed that the same size-independent specific fracture energy can also be obtained by testing only two specimens of the same size but with notches which are well separated. Their method greatly reduces the number of test specimens and simplifies the determination of G_F. In a recent paper, the first of its kind, Cifuentes *et al*. showed that if the size-dependent G_f measured by the RILEM method is corrected following the methods of Elices and co-workers (Elices *et al*. 1992, Guinea *et al*. 1992, Planas *et*

al. 1992 **)** and Hu and Wittmann (2000) or its simplification proposed by Karihaloo *et al*. (2003), if the notch to depth ratios are well separated), then the resulting specific fracture energy G_F is very nearly the same and independent of the size of the specimen. They reached this important conclusion on the basis of a very limited set of results on a single concrete mix of compressive strength 37 MPa.

The tension softening diagram of concrete, which is one of the fracture mechanics parameters, is defined as the relationship between tensile stress and crack width ($\sigma(w)$) in the fracture process zone. The fracture energy is obtained as the area under the tension softening diagram. The tension softening diagram can describe the post-cracking behavior and express the resistance of concrete against crack development. In practice, the $\sigma(w)$ relationship is generally assumed as linear, bilinear, polylinear or even exponential curve with the bilinear approximation being the most common (Karihaloo 1995). The popularity of the bilinear approximation of the tension softening diagram (TSD) stems from the fact that it captures the two major mechanisms responsible for the observed tension softening in concrete, namely microcracking and aggregate interlock. The initial, steep branch of the bilinear TSD is a result of microcracking, whereas the second, tail branch is a result of aggregate interlock.

This paper will provide an insight on the various mechanical properties such as compressive strength, split tensile strength, modulus of elasticity, size dependent fracture energy, size independent fracture energy, tensile stress vs crack width by using test results of three different concrete mixes ranging in compressive strength from 57 to 122 MPa.

1.1 Size dependent specific fracture energy (G_f)

Fracture energy, G_f is an important material parameter can be seen as a measure for the ductility of concrete. The fracture energy, G_f is defined as the amount of energy necessary to create a crack of unit surface area projected in a plane parallel to the crack direction.

The area under the load-displacement plot is considered as the work of fracture (W_F) and is defined as

$$W_F(w) = \int_0^w P\, d\,w \tag{1}$$

where "w" is the crack mouth opening displacement, W_F is the work of fracture, P is the applied load.

According to RILEM method of Hillerborg, the fracture energy G_f is the average energy given by dividing the total work of fracture by the projected fracture area (RILEM 1985). In case of a specimen of depth W, initial crack length a_0, and thickness t, the fracture energy is given by

$$G_f = \frac{W_F}{(W - a_0)t} \tag{2}$$

1.2 Size independent fracture energy by Boundary effect method (BEM)

In this paper, size independent specific fracture energy has been determined by using boundary

effect method. Hu and Wittmann (1992) observed that the effect of the stress-free back boundary of the specimen is felt in the fracture process zone (FPZ) ahead of a real growing crack. The local fracture energy varies with the width of the fracture process zone. As the crack approaches the back stress-free face of the specimen the fracture process zone becomes more and more confined and hence the local fracture energy decreases (Hu and Wittmann 2000). Initially, when the crack grows from a pre-existing notch, the rate of decrease is negligible, but it accelerates as the crack approaches the end of the un-cracked ligament. This change in the local fracture energy (g_f) is approximated by a bilinear function, as shown in Fig. 1. The transition from horizontal line to the sharply inclined line occurs at the transition ligament length, which depends on the material properties and specimen size and shape. In the boundary effect model of Hu and Wittmann (2000), the measured RILEM fracture energy, G_f, may be regarded as the average of the local fracture energy function (dotted line in Fig. 1) over the initial un-cracked ligament area. The relationship between all the involved variables is given by

$$G_f(a,W) = \frac{\int_0^{W-a} g_f(x)dx}{W-a} = \begin{cases} G_F\left[1 - \dfrac{a^*_l / W}{2(1-a/W)}\right]; & 1 - a/W > a^*_l / W \\ G_F \dfrac{2(1-a/W)}{2a^*_l / W}; & 1 - a/W \le a^*_l / W \end{cases} \quad (3)$$

in which G_f is the specific fracture energy or size dependent fracture energy (RILEM), G_F is the true or size-independent fracture energy, W is the overall depth of the beam, a is the initial notch depth and a^*_l is the transition ligament length.

To obtain the values of G_F and a^*_l of a concrete mix, the size-dependent specific fracture energy G_f of specimens of different sizes and a range of the notch to depth ratios is first determined by the RILEM work-of-fracture method. Then Eq. (3) is applied to each specimen depth and notch to depth ratio. This gives an over-determined system of equations which is solved by a least squares method to obtain the best estimates of G_F and a^*_l.

2. Construction of tension softening diagram

An analytical model based on the concept of a nonlinear hinge was proposed by Ulfkjaer (1995) in which the flexural response of concrete beams was modelled by the development of a fictitious crack in the central region of the beam subjected to the maximum bending moment. The width of this region, proportional to the beam depth, fixes the width of the non-linear hinge. It was assumed that $\sigma(w)$ is linear. This model was further developed by Stang and Olesen (1998) and Olesen (2001) to demonstrate its applicability to three point bend (TPB) beams using a bilinear approximation for $\sigma(w)$. During the inverse analysis, a load versus crack mouth opening displacement (P-CMOD) curve is obtained for each trial σ - w curve, defined by a set of parameters and compared with the corresponding experimental results. The advantage of the hinge model is that it yields closed-form analytical solutions for the entire load-crack opening displacement curve. In the fictitious crack model, it is assumed that prior to crack initiation, the material exhibits linear elastic behaviour. After crack initiation, it is assumed that stresses may be transmitted across the crack, hence the crack is termed as a fictitious crack. The crack bridging

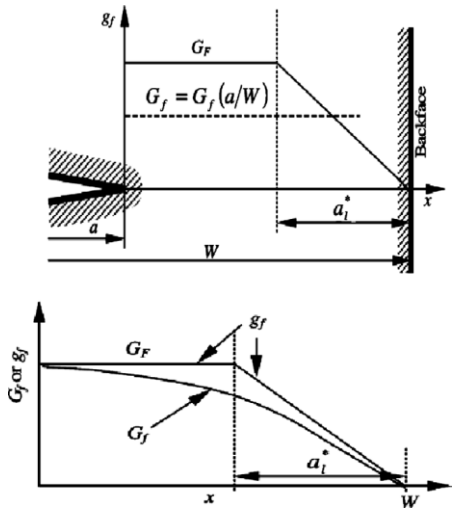

Fig. 1 Variation of local fracture energy g_f and G_F over the ligament length (Karihaloo *et al*. 2003)

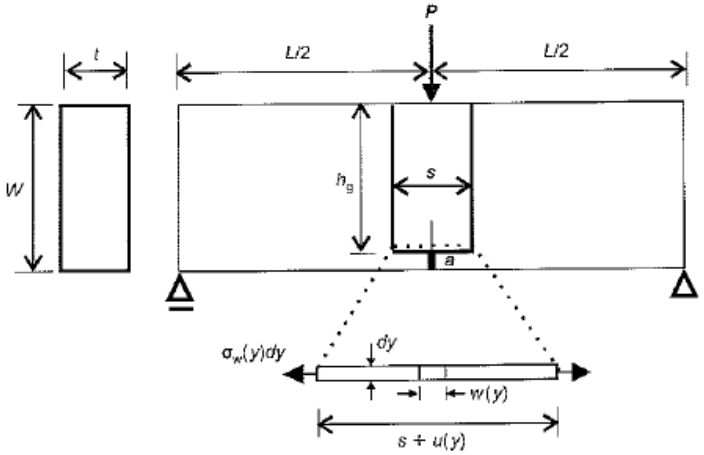

Fig. 2 Three-point notched bend beam with a non-linear hinge modelling the propagation of a crack at mid-section (Abdalla and Karihaloo 2004)

forces are taken to be a function of the crack opening displacement given by the stress-crack opening relationship. The bending failure of concrete beams may be modeled by the development of a fictitious crack in an elastic layer with a thickness proportional to the beam depth. The basic idea of the non-linear cracked hinge model is to isolate the part of the beam close to the propagating crack (i.e., the part under maximum bending moment) as a short beam segment subjected to a bending moment and normal force. Fig. 2 shows a typical TPB specimen. In the non-linear hinge model the crack is viewed as a local change in the overall stress and strain field. This change is assumed to vanish outside a certain band of width *s* (Refer Fig. 2). Thus, outside of this band the structural element is modelled using the elastic beam theory. The boundaries of the hinge are assumed to be rigid and may rotate and translate. The constitutive relationship for each

segment inside the hinge is assumed to be linear elastic in the precracked state (phase 0), while the cracked state is approximated by a bilinear softening curve as shown in Fig. 3

$$\sigma = \begin{cases} E\varepsilon & pre\text{-}cracked\ \ state \\ \sigma(w) = g(w) f_t & cracked\ state \end{cases} \tag{4}$$

where E is the elastic modulus; ε is the elastic strain; w is the crack opening; f_t is the uniaxial tensile strength; and $g(w)$ is the function representing the shape of the stress-crack opening relationship, normalised such that $g(0) = 1$. For the assumed bilinear shape (Fig. 3) we have

$$g(w) = b_i - a_i w = \begin{cases} b_1 - a_1 w, 0 \le w \le w_1 \\ b_2 - a_2 w, w_1 \le w \le w_2 \end{cases} \tag{5}$$

$$w_1 = \frac{1 - b_2}{a_1 - a_2} \tag{6a}$$

$$w_2 = \frac{b_2}{a_2} \tag{6b}$$

where $b_1 = 1$; and the limits w_1 and w_2 are given by the intersection of the two line segments, and the intersection of the second line segment with the abscissa, respectively (refer Fig. 3).

The complete details of inverse analysis and evaluation of bi-linear parameters can be found in literature (Ulfkjaer *et al*. 1995, Stang and Olesen 1998, Olesen 2001, Abdalla and Karihaloo 2004,

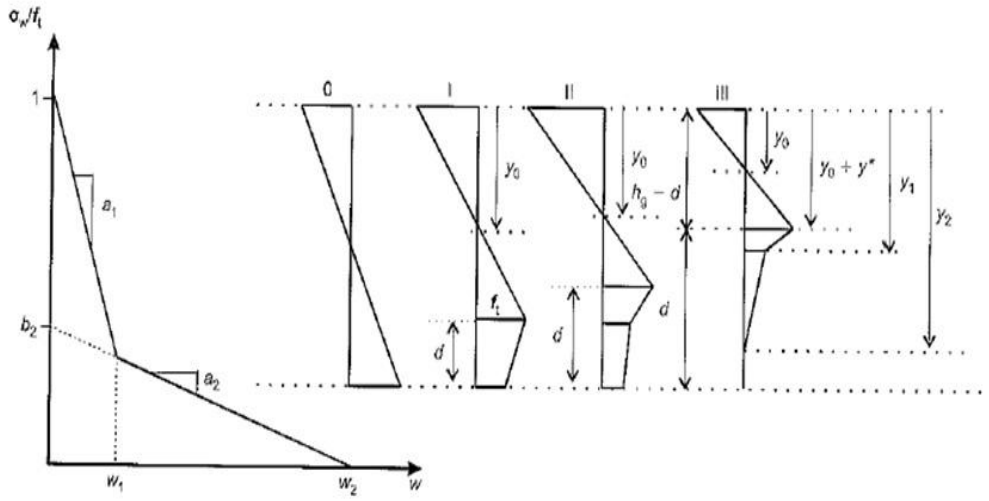

Fig. 3 Three-point notched bend beam with a non-linear hinge modelling the propagation of a crack at mid-section (Abdalla and Karihaloo 2004)

Ostergaard 2003). But the important point to note is the tension softening diagram and the bi-linear parameters obtained from inverse analysis are corresponding to size dependent fracture energy. The parameters obtained from inverse analysis have been modified as per the procedure given by Abdalla and Karihaloo (2004) so that they correspond to the true G_F of the concrete mix that is independent of the shape and size of the test specimen.

3. Experimental investigation

Prismatic notched specimens were subjected to three-point bending in accordance with the RILEM procedure (1995). Table 1 gives the geometrical dimensions of all test specimens (Ramachandra Murthy 2011). Properties of the materials used to make normal strength concrete (NSC), high strength concrete (HSC) and ultra high strength concrete (UHSC) are given below.

Cement
•Grade - 53 (OPC)
•Particle size range - 31 µm to 7.5 µm
•Compressive strength at 28 days - 57 MPa
Silica fume (SF)
•Particle size range - 0.2 to 25µm
Quartz powder (QP)
•Particle size range - 2.3 µm to 75 µm
Quartz sand
•Particle size range - 400 µm to 800 µm
Steel fibers
•Length - 13 mm
•Diameter - 0.18 mm
•Yield stress - 1500 MPa
Standard sand
•Particle size range - 0.5 mm to 0.09 mm (Grade 3 of IS:650)
Coarse aggregate
•Particle size range - 4.75 mm to 20 mm

3.1 Super plasticizers (SP)

Polycarboxylate ether based superplasticizer is used. Appearance of SP is light yellow coloured liquid.

The materials and mix proportions used in NSC, HSC and UHSC are given in Table 2. The specimen preparation was strictly controlled to minimize the scatter in the test results. The NSC specimens were demoulded after 1 day and cured in a water tank at ambient temperature for 28 days. The HSC and UHSC specimens were also demoulded after 1 day and immersed in water at ambient temperature for 2 days. They were then placed in an autoclave at 90℃ for 2 days and in an oven at 200℃ for 1 day. Thereafter they were air cooled for 6 hours and placed in water at ambient temperature for a further 1 day before testing. Compression and split tensile tests were carried out on cylindrical specimens of 150 × 300 mm (diameter×height) in the case of NSC and

Table 1 Geometrical properties of the notched specimens

Mix	Beam dimensions (mm) (Length × width × depth)	Notch to depth ratio
NSC	250 × 50 × 50	0.1
		0.2
		0.3
	500 × 50 × 100	0.1
		0.2
		0.3
	1000 × 50 × 200	0.1
		0.2
		0.3
HSC	250 × 50 × 50	0.1
		0.2
		0.3
		0.4
	500 × 50 × 100	0.1
		0.2
		0.3
		0.4
UHSC	250 × 50 × 50	0.1
		0.2
		0.3
		0.4
	400 × 50 × 80	0.1
		0.2
		0.3
		0.4
	650 × 50 × 130	0.1
		0.2
		0.3
		0.4

Table 2 Mix proportions by mass (except for steel fiber which is by volume) of NSC, HSC and UHSC

Mix	Cement	Fine aggre-gate	Coarse aggre-gate	Silica fume	Quartz sand	Quartz powder	Steel fiber by vol. (length = 13 mm dia.=0.18 mm)	w/c	SP %
NSC	1	1.25	2.48	-	-	-	-	0.45	-
HSC	1	-	-	0.25	1.5	-	2%	0.33	2.5
UHSC	1	-	-	0.25	1.1	0.4	2%	0.23	3.5

Fig. 4 Typical notched beam specimens

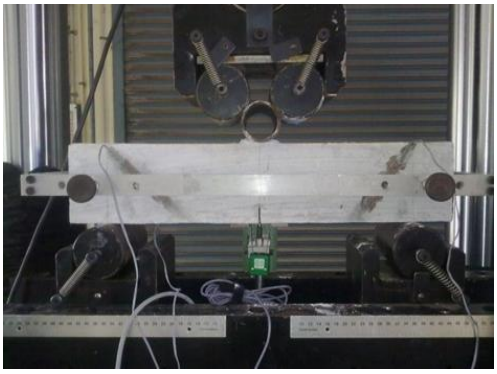

Fig. 5 Part of experimental set-up

(a)NSC -250 × 50 × 50 (notch depth = 5 mm)

(b) HSC – 500 × 50 × 100 (notch depth =20 mm)

(c) UHSC – 650 × 50 × 130 (notch depth = 13 mm)

Fig. 6 Typical failure pattern of beams

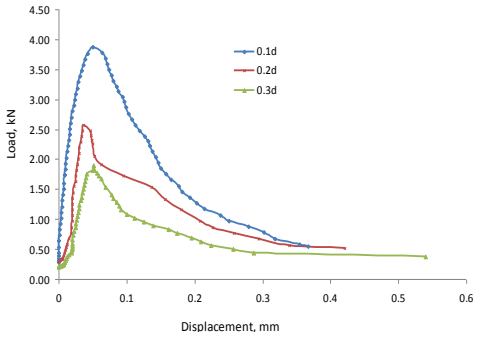

(a) NSC – 500 × 50 × 100 mm

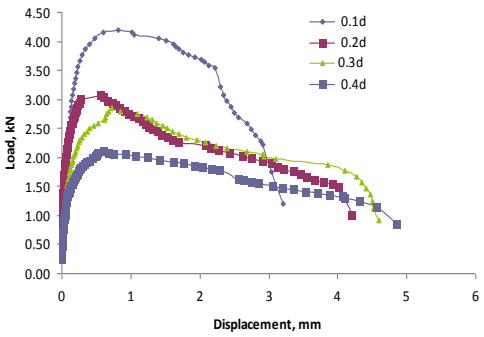

(b) HSC – 250 × 50 × 50 mm

Fig. 7 Typical Load –displacement plots

Table 3 Mechanical properties of NSC, HSC and UHSC

Mix	Cylinder compressive Strength (MPa)	Split tensile strength (MPa)	Modulus of elasticity (GPa)
NSC	57.1	4.0	35.8
HSC	87.7	15.4	37.9
UHSC	122.5	20.7	43.0

on smaller cylinders 75 × 150 mm in the case of HSC and UHSC. Various mechanical properties such as compressive strength, spilt tensile strength and modulus of elasticity of NSC, HSC and UHSC mix at 28 days are shown in Table 3. From Table 3, it can be observed that the split tensile strength for the case of NSC is 4.0 MPa. It is about 7% of compressive strength. In the case of HSC, the split tensile strength is about 18% of compressive strength. The increase in strength is significant compared to NSC. The increase in strength may be due to various sizes of ingredients and steel fibres. Further, it can be observed from Table 3 that UHSC has high compressive strength and tensile strength. The high strengths can be attributed to the contribution at different scales viz., at the meso scale due to the fibers and at the micro scale due to the close packing of grains which is on account of good grading of the particles. Notches (width approximately 3 mm) of various depths given in Table 1 were cut in beam specimens using a diamond saw. Four identical specimens for each beam size and each notch depth were cast (Fig. 4). All tests were performed in a closed-loop servo-hydraulic testing machine, controlled by the crack mouth opening displacement (CMOD) measured with a clip gauge (Fig. 5). A linearly varying displacement transducer (LVDT) was used to measure the the mid-span vertical displacement, δ. The load-CMOD and load-displacement curves of all specimens were recorded. The ratio of the span between the supports to the depth of the specimen was maintained at 4 for all specimens. The pictorial representation of the typical failure pattern of NSC, HSC and UHSC beams is shown in Fig. 6. From the failure pattern of HSC and UHSC beams, it was noted that the nature of failure is ductile which is reflected by the structural integrity of the member till the crack propagated up to 90% of the beam depth.

Typical load-displacement and load –crack mouth opening displacement curves are shown Figs. 7 and 8. From Figs. 7 and 8, it can be noted that while NSC specimens behave like quasi brittle material, HSC and UHSC specimens behave elastically for a higher range of displacement compared to NSC beams. This could be due to that while the addition of quartz powder/quartz sand imparts homogeneous brittle failure, the presence of steel fibers which are randomly oriented increased the tension capacity through crack bridging. From Fig. 8, it can be observed that the critical CMOD in the case of NSC beams ranges from 0.15 to 0.5 mm. In the case of HSC and UHSC, it is in the order of 4 mm. It is worth highlighting the fact that the CMOD of 4 mm is the maximum that the clip guage could measure. In fact, much larger value of the CMOD could have been observed with a larger clip gauge. Hence, it can be noted that HSC and UHSC beams can withstand for larger deformations which shows the ductile nature.

Tables 4 to 6 show the mean values of the specific fracture energy G_f obtained from the three-point bend tests of NSC, HSC and UHSC specimens according to the RILEM procedure. An inspection of the entries in column 3 of Tables 4 to 6 highlights the dependency of the RILEM specific fracture energy on the notch depth or the size of the un-cracked ligament. The specific fracture energy increases with an increase in the beam depth for the same notch to depth ratio and it decreases with an increase in the notch to depth ratio for the same beam depth. For the NSC used in the present investigation it varied between 57.8 N/m for a specimen with W = 50 mm and a/W = 0.3 to 153.0 N/m for a specimen with W = 200 mm and a/W = 0.1 (Table 4). For the HSC (Table 5) it varied between 2923.0 N/m (W = 50 mm, a/W = 0.4) and 4396.3 N/m (W = 100 mm, a/W = 0.1) and for the UHSC (Table 6) between 4406.3 N/m (W = 50 mm, a/W = 0.4) and 11945.3 N/m (W = 130 mm, a/W = 0.1).

Tables 4 to 6 also give the size-independent specific fracture energy (G_F) and transition ligament length a_l obtained by solving the over-determined system of equations obtained by substituting $G_f(a/W;W)$ from Tables 4-6 for each W into Eq. (3) of boundary effect method.

Table 4 Mean fracture energy and coefficient of variation, and size independent specific fracture energy of NSC

Beam dimensions, mm	Notch to depth ratio	Mean fracture energy, G_f, as per RILEM N/m	Size independent fracture energy, G_F, N/m	Transition ligament length, a_l, mm
250 × 50 × 50	0.1	117.3 ± 3.29%	188.2	34.5
	0.2	85.3 ± 9.03%		
	0.3	57.8 ± 15.44%		
500 × 50 × 100	0.1	135.3 ± 4.73%	190.3	68.3
	0.2	107.5 ± 10.23%		
	0.3	95.5 ± 4.87%		
1000 ×50 × 200	0.1	153.0 ± 5.57%	192.3	95.4
	0.2	126.3 ± 10.91%		
	0.3	109.3 ± 4.38%		

Table 5 Mean fracture energy and coefficient of variation, and size independent specific fracture energy of HSC

Beam dimensions, mm	Notch to depth ratio	Mean fracture energy, G_f, N/m	Size independent fracture energy, G_F, N/m	Transition ligament length, a_l, mm
250 × 50 × 50	0.1	4109.5 ± 1.03%	6385.2	27.3
	0.2	3679.8 ± 4.91%		
	0.3	3479.8 ± 4.71%		
	0.4	2923.0 ± 1.54%		
500 × 50 × 100	0.1	4396.3 ± 6.91%	6401.0	51.2
	0.2	4155.3 ± 7.22%		
	0.3	4020.0 ± 10.95%		
	0.4	3397.0 ± 13.01%		

Table 6 Mean fracture energy and coefficient of variation, and size independent specific fracture energy of UHSC

Beam dimensions, mm	Notch to depth ratio	Mean fracture energy, G_f, N/m	Size independent fracture energy, G_F, N/m	Transition ligament length, a_l, mm
250 × 50 × 50	0.1	10405.3 ± 0.66%	14103.1	24.3
	0.2	8148.5 ± 2.17%		
	0.3	6798.8 ± 1.55%		
	0.4	4406.3 ± 2.67%		
400 ×50 × 80	0.1	11452.8 ± 0.73%	14212.8	41.2
	0.2	8733.8 ± 1.32%		
	0.3	7036.8 ± 2.03%		
	0.4	4976.8 ± 1.98%		
650 × 50 × 130	0.1	11945.3 ± 0.76%	14238.6	54.2
	0.2	8306.8 ± 4.72%		
	0.3	6981.5 ± 1.16%		
	0.4	5961.5 ± 1.78%		

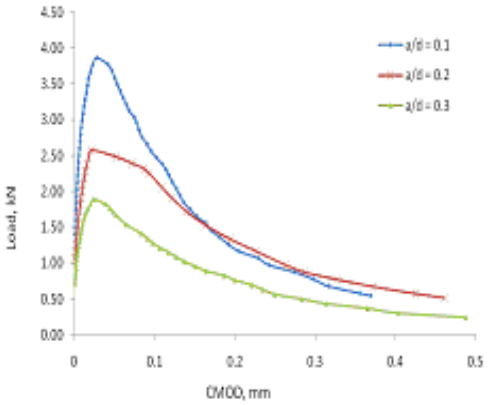

(a) NSC – Small size beam

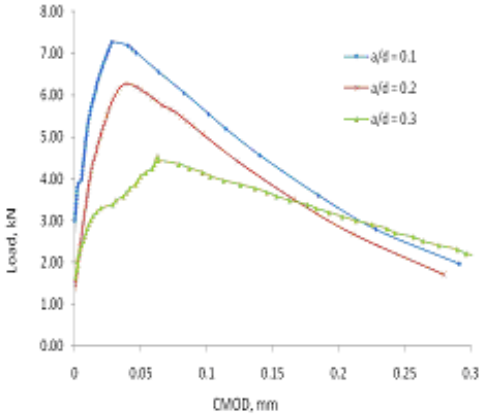

(b) NSC – Large size beam

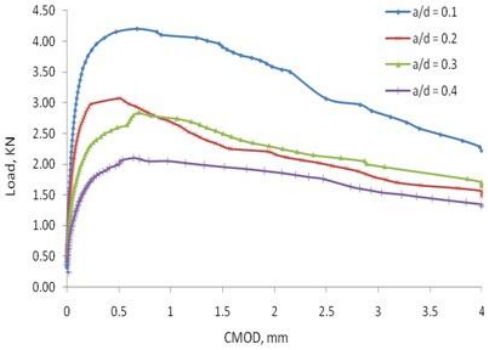

(c) HSC – Small size beam

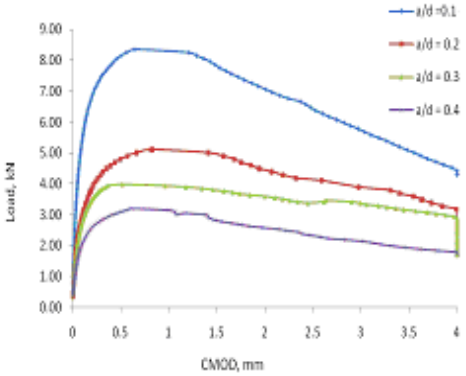

(d) HSC – Medium size beam

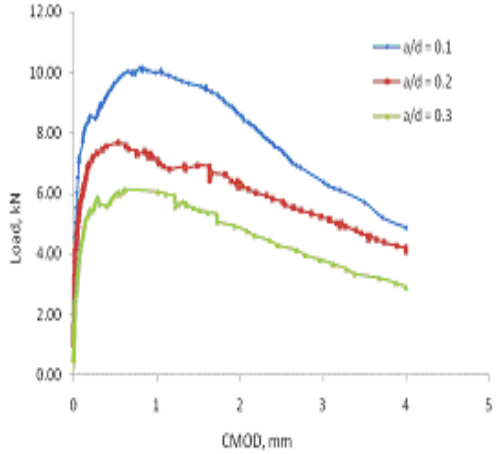

(e) UHSC – Small size beam

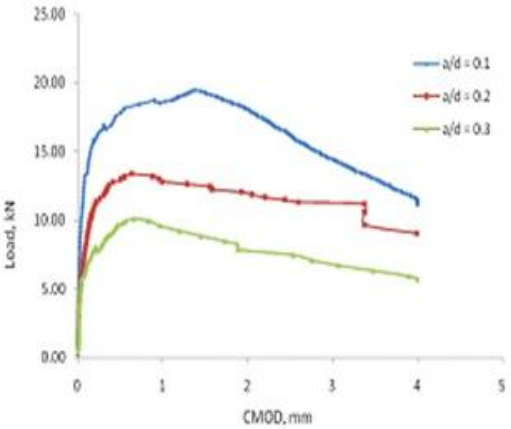

(f) UHSC – Large size beam

Fig. 8 Typical load-CMOD plots

Table 7 Elastic properties and parameters of the bilinear softening diagram corresponding to the size independent fracture energy G_F

Mix	f_c, MPa	f_t, MPa	E, GPa	a_1, mm^{-1}	a_2, mm^{-1}	b_2	w_1, mm	w_2, mm	σ_1, MPa	G_F, N/m
NSC	57.1	2.60	35.8	5.495	2.295	0.727	0.085	0.317	1.382	184.5
HSC	87.7	10.01	37.9	0.989	0.134	0.404	0.697	3.018	3.113	6194.7
UHSC	122.5	13.455	43.0	0.640	0.144	0.546	0.915	3.786	5.566	13760.7

Table 8 Characteristics length and brittleness number for NSC, HSC and UHSC

Mix	l_{ch} (mm)	Brittleness number			
		W = 150	W = 200	W = 300	W = 500
NSC	840.20	5.6	4.20	2.80	1.68
HSC	2342.8	15.61	11.71	7.80	4.68
UHSC	3268.51	21.79	16.34	10.89	6.53

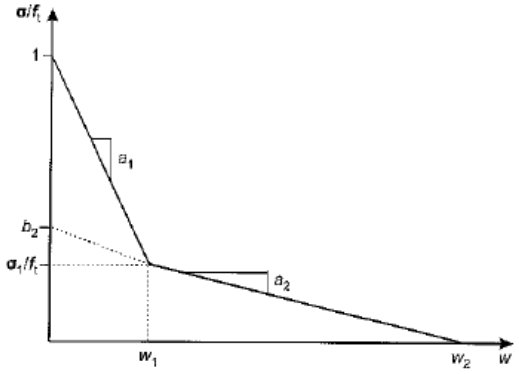

Fig. 9 Bilinear tension softening diagram

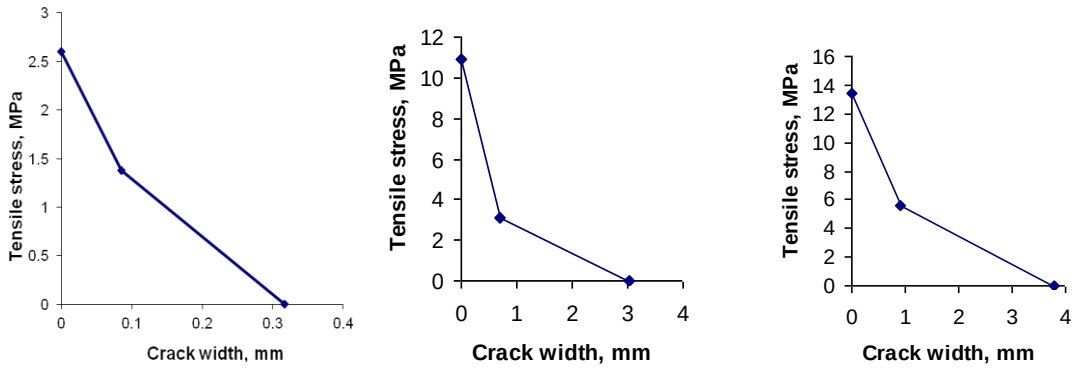

Fig. 10 Bilinear stress—crack opening relationship for NSC, HSC and UHSC corresponding to their true fracture energy G_F

It is important to note that the solution of this over-determined system by the method of least squares may require the explicit imposition of the inequality constraint on a_l/W that appears in Eq. (1) in order to obtain the best estimates of G_F and a_l (Ramachandra Murthy *et al*. 2013).

It should also be noted that the simplified boundary effect method proposed by Karihaloo *et al*. (Karihaloo *et al*. 2003) cannot be used on the above test specimens because the notch to depth ratios are closely spaced and not well separated, as required by the simplified BEM. From Tables 4 to 6, it is clear that G_F values are almost the same for a particular mix i.e., NSC, HSC or UHSC irrespective of specimen size and notch depth.

The area under the softening curve obtained using the hinge model is not equal to G_F but to the measured $G_f(\alpha, W)$. It can be observed that the area under the bilinear TSD is generally less than the true G_F. Thus the true G_F of the NSC, HSC and UHSC are 190.27 N/m, 6393.1 N/m and 14184.7 N/m respectively [Tables 4 - 6] whereas the average area under the bilinear TSD is only 109.7 N/m for the case of NSC, 3770.1 N/m for HSC and 7929.5 N/m for UHSC.

The size-dependent fracture energy (i.e., the area under the bilinear TSD) is given by (Fig. 9)

$$G_f^*(\alpha, W) = \frac{1}{2} f_t^* \left(w_1^* + \frac{\sigma_1^*}{f_t^*} w_2^* \right) \tag{7}$$

where the superscript * denotes the average parameters of the bilinear diagram obtained from the hinge model.

where w_1, w_2 and σ_1, which are to be determined, are the bilinear diagram parameters corresponding to the true fracture energy G_F, and f_t is the direct tensile strength of the mix obtained from an independent test, say a split cylinder test, f_{st}.

The parameters of the bilinear TSD corresponding to the true G_F values of three concrete mixes have been obtained as per the procedure given by Abdalla and Karihaloo (2004) and are shown in Table 7. The TSDs are plotted in Fig. 10.

The size-independent fracture energy (i.e., the area under the bilinear TSD corresponding to G_F) can similarly be written as

$$G_F = \frac{1}{2} f_t \left(w_1 + \frac{\sigma_1}{f_t} w_2 \right) \tag{8}$$

Fig. 11 Samples for micro-indentation

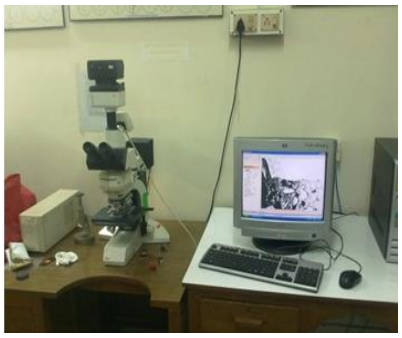

Fig. 12 Metallurgical microscope

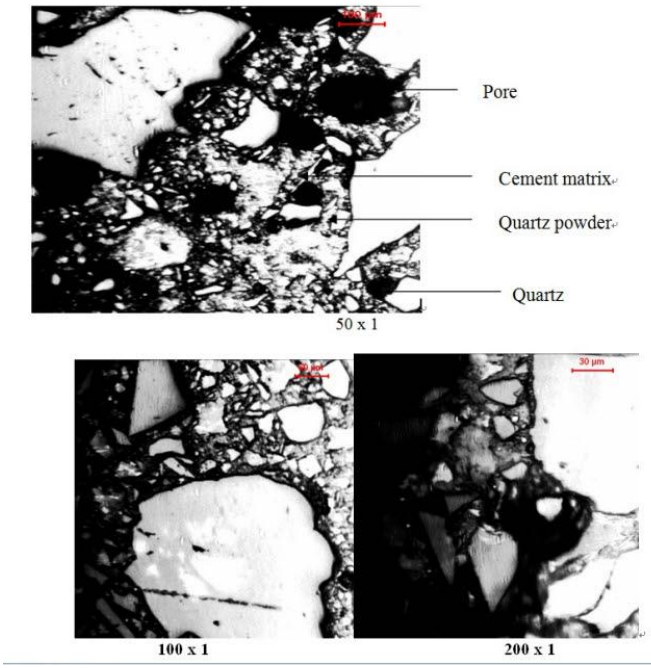

Fig. 13 Micro-structure of UHSC

4. Microstructure of UHSC

Specimens having diameter of 50 mm and thickness of 10 mm have been prepared from UHSC mix. After heat treatment of the samples, dry polishing has been carried out by using 100, 180, 240, 320, 400, 600, 800 and 1000 grit silicon carbide papers. Further, polishing has been done with rotating cloth and diamond lapping film. Fig. 11 shows the samples prepared for micro indentation and micro structure. Fig. 12 shows the schematic set-up of metallurgical microscope.

Fig. 13 shows the typical micro-structure of UHSC specimen for various magnification levels such as 50, 100 and 200. From Fig. 13, it can be observed that there are some more pores/voids in the matrix of UHSC. There is scope to further improve the micro-structure of UHSC by adding cementitious/pozzolanic materials.

4.1 Characteristic length

Characteristic length (l_{ch}) is a property of a mix and it is a derived quantity. It can be obtained by using the following expression.

$$l_{ch} = \frac{EG_f}{f_t^z} \tag{9}$$

where, E = Modulus of elasticity

G_F = Size independent fracture energy

f_t = Tensile strength corresponding to G_F

4.2 Brittleness number

Brittleness number is related to not only material but also geometry and size of the structure

$$\beta = \frac{l_{ch}}{W} \tag{10}$$

where, W = characteristics size of the structure

Table 8 shows characteristics length and brittleness number for NSC, HSC and UHSC. From Table 8, it can be noted that for a particular beam size, brittleness number is decreasing with increase of beam size for all the mixes. Characteristic length (l_{ch}) is found to be larger for HSC and

5. Conclusions

Characterization and tests on notched three point bend specimens of three different concrete mixes ranging in compressive strength from 57 to 122 MPa have been carried out. Various mechanical properties such as compressive strength, split tensile strength, modulus of elasticity, fracture energy and tensile stress vs crack width have been obtained from test results. The following conclusions are drawn from extensive experimental results:

• The high compressive strength and tensile strength of UHSC can be attributed to the contribution at different scales viz., at the meso scale due to the fibers and at the micro scale due to the close packing of grains which is on account of good grading of the particles.

• The specific fracture energy obtained from RILEM work of fracture method increases with an increase in the beam depth for the same notch to depth ratio and it decreases with an increase in the notch to depth ratio for the same beam depth

• The size independent specific fracture energy obtained from boundary effect of method of Hu and Wittmann (1992,2000), are almost the same for a particular mix i.e., NSC, HSC or UHSC irrespective of specimen size and notch depth.

• The parameters of bi-linear tension softening diagram have been obtained through inverse analysis and have been modified corresponding to true specific fracture energy as per the procedure given by Abdalla and Karihaloo (2004).

Micro structure of UHSC mix, characteristic length and brittleness number has been discussed briefly**.**

Acknowledgements

The valuable technical suggestions and support provided by our colleagues and the help by the staff of Advanced Materials Laboratory, CSIR-SERC to carry out the experiments is greatly

acknowledged. This paper is being published with the permission of the Director, SERC, Chennai, India.

Reference

Richard, P. and Cheyrezy. M.H. (1994), "Reactive powder concretes with high ductility and 200-800 MPa compressive strength", *ACI SP144*, **24**, 507-518.

Richard, P. and Cheyrezy. M.H. (1995), "Composition of reactive powder concretes", *Cement Concrete Res*., **25**(7), 1501-1511.

Mingzhe, A.N., Ziruo, Y.U., Sun, M., Zheng, S. and Liang, L. (2010), "Fatigue properties of RPC under cyclic loads of single-stage and multi-level amplitude", *Journal of Wuhan University of Technology-Material Science Ed*., 167-173.

Goltermann, P., Johansen, V. and Palbol, L. (1997), "Packing of aggregates: an alternate tool to determine the optimal aggregate mix", *ACI Mater. J*., 435-443.

Massidda, L., Sanna, U., Cocco, E. and Meloni, P. (2001), "High pressure steam curing of reactive-powder mortars", *ACI SP200-27*, **200**, 447-464.

Guvensoy, G., Bayramov, F., Ilki, A., Sengül, C., Tasdemir, M.A., Kocatürk, A.N. and Yerlikaya, M. (2004), "Mechanical behavior of high performance steel fiber reinforced cementitious composites under cyclic loading condition", ultra high performance concrete (UHPC). In: *International Symposium on Ultra High Performance Concrete*, **13**, 649-660.

Chan, Y.W. and Chu., S.H. (2004), "Effect of silica fume on steel fiber bond characteristics in reactive powder concrete", *Cement Concrete Res*., **34**, 1167-1172.

Shaheen, E. and Shrive, N. (2006), "Optimization of mechanical properties and durability of reactive powder concrete", *ACI Mater. J*., **103**, 444-451.

Lee, M.G., Wang, Y.C. and Chiu, C.T. (2007), "A preliminary study of reactive powder concrete as a new repair material", *Construct. Build. Mater*., **21**, 182-189.

Wang, Y.C. and Lee, M.G. (2007), "Ultra-high strength steel fiber Reinforced concrete for strengthening of RC frames", *J. Marine Scie. Tech*., **15**(3), 210-218.

Yazıcı, H., Mert, Y.Y., Serdar, A., and Anıl, S.K. (2009), "Mechanical properties of reactive powder concrete containing mineral admixtures under different curing regimes", *Construct. Build. Mater*., **23**, 1223-1231.

RILEM (1985), "Determination of the fracture energy of mortar and concrete by means of three-point bend tests on notched beams", *Mater. Struct*., **18,** 99-101(prepared by TC50-FMC).

Pan, Z. (2011), "Fracture properties of geopolymer paste and concrete", *Mag. Concr. Res*., **63,** 763-771.

Sahin, Y. and Koksal, F. (2011), "The influences of matrix and steel fibre tensile strengths on the fracture energy of high strength concrete", *Constr. Build. Mater*., **25**, 1801-1806.

Bazant, Z.P. and Kazemi, M.T. (1991), "Size dependence of concrete fracture energy determined by RILEM work-of-fracture method", *Int. J. Fract*., **51,** 121-138.

azant, Z.P. (1996), "Analysis of work-of-fracture method for measuring fracture energy of concrete", *ASCE J. Mater. Civil Eng*., **122**, 138-144.

Nallathambi, P., Karihaloo, B.L. and Heaton, B.S. (1985), "Various size effects in fracture of concrete", *Cement Concrete Res*., **15**, 117-126.

Carpinteri, A. and Chiaia, B. (1996), "Size effects on concrete fracture energy: dimensional transition from order to disorder", *Mater. Struct*., **29**, 259-266.

Hu, X. and Wittmann, F. (1992), "Fracture energy and fracture process zone", *Mater. Struct*., **25**, 319-326.

Elices, M., Guinea, G.V. and Planas, J. (1992), "Measurement of the fracture energy using three-point bend tests: part 3—Influence of cutting the P - δ tail", *Mater. Struct*., **25**, 137-163.

Guinea, G.V., Planas, J. and Elices, M. (1992), "Measurement of the fracture energy using three-point bend tests: part 1—Influence of experimental procedures", *Mater. Struct*., **25**, 212-218.

Planas, J., Elices, M. and Guinea, G.V. (1992), "Measurement of the fracture energy using three-point bend

tests: part 2—Influence of bulk energy dissipation", *Mater. Struct.*, **25**, 305-312.
Hu, X. and Wittmann, F. (2000), "Size effect on toughness induced by crack close to free surface", *Eng. Fract. Mech.*, **65**, 209-221.
Karihaloo, B.L., Abdalla, H.M. and Imjai, T. (2003), "A simple method for determining the true specific fracture energy of concrete", *Mag. Concr. Res.*, **55**, 471-481.
Abdalla, H.M. and Karihaloo, B.L. (2003), "Determination of size-independent specific fracture energy of concrete from three-point bend and wedge splitting tests", *Mag. Concr. Res.*, **55**, 133-141.
Cifuentes, H., Alcalde, M. and Medina, F. (2012), "Measuring the size independent fracture energy of concrete", *Strain*.
Karihaloo, B.L. (1995), "Fracture mechanics and structural concrete", Longman Scientific & Technical, U.K.
Ulfkjaer, J.P., Krenk, S. and Brincker, R. (1995), "Analytical model for fictitious crack propagation in concrete beams", *J. Eng. Mech. - ASCE* , **121**, 7-15.
Stang, H. and Olesen, J.F. (1998), "On the interpretation of bending tests on FRC-materials. Proceedings of FRAMCOS-3, Fracture Mechanics of Concrete Structures", Aedificatio Publishers. Freiburg, Germany, **I**, 511-520.
Olesen, J.F. (2001), "Fictitious crack propagation in fiber-reinforced concrete beams", *J. Eng. Mech. – ASCE* , **127**, 272-280.
Abdalla, H.M. and Karihaloo, B.L. (2004), "A method for constructing the bilinear tension softening diagram of concrete corresponding to its true fracture energy", *Mag. Concr. Res.*, **56,** 597-604.
Ostergaard, L. (2003), "Early-age fracture mechanics and cracking of concrete", Ph.D. Thesis, The Technical University of Denmark, Lyngby.
Ramachandra Murthy, A. (2011), "Fatigue and fracture behaviour of ultra high strength concrete beams", Ph.D. Thesis, Indian Institute of Science, Bangalore, India.
Ramachandra Murthy, A., Karihaloo, B.L., Nagesh, R.I. and Raghu Prasad, B.K. (2013), "Determination of size-independent specific fracture energy of concrete mixes by two methods", *Cement Concrete Res.*, **50,** 19-25.

CC